A method to assess the cloud-aerosol transition zone from ceilometer measurements

Jaume Ruiz de Morales [a,*], Josep Calbó [a], Josep-Abel González [a], Yolanda Sola [b]

[a] *Grup de Física Ambiental, Departament de Física, Universitat de Girona, Catalonia, Spain*
[b] *Grup de Meteorologia, Departament de Física Aplicada, Universitat de Barcelona, Catalonia, Spain*

ARTICLE INFO

ABSTRACT

Cloud and aerosol contribution to the Earth's radiative budget constitutes one of the most significant uncertainties in future climate projections. To distinguish between clouds and cloud-free air, atmospheric scientists have been using a wide range of instruments, techniques, and algorithms with various detection thresholds. However, since the change from a cloudy to a cloud-free atmosphere may be gradual and, in some cases, far from obvious, recent research is questioning where the threshold between both phases should be established. These considerations lead to contemplate a transition zone (TZ) between cloud and cloud-free conditions. In the present study, backscatter profiles obtained by a Vaisala CL31 ceilometer were processed to assess the transition zone. First, two widely used cloud detection algorithms were applied and compared: the method provided by the ceilometer manufacturer (Vaisala) and Cloudnetpy, the algorithm from ACTRIS Cloudnet, a project devoted to aerosol, clouds, and trace gases research. Second, a sensitivity analysis was applied to the backscatter and signal-to-noise ratio thresholds used for cloud detection in Cloudnetpy. This methodology has allowed us to assess the vertical distribution of clouds, aerosols, the TZ, and its frequency of occurrence. Results indicate a gradual transition in backscatter retrievals from cloud to cloud-free, where particles detected near cloud boundaries induced higher backscatter values than those found further away. Depending on the thresholds used, we observed a 9.3% (with an estimated range of uncertainty of 5.4—20%) variation in cloud occurrence which can be attributed to TZ conditions. Analysing the whole backscatter profile, we found as many TZ conditions as cloudy values, which emphasises the importance of studying the vertical distribution of the TZ. Moreover, the analysis of TZ occurrence in height and time revealed that such conditions concentrate below 800 m during night periods, although annual height-hour distributions involve a remarkable variability among seasons. These findings highlight the importance of either including an additional phase between 'pure clouds' and 'pure aerosols' or treating them as a continuum of suspended particles in the atmosphere.

1. Introduction

Aggregates of suspended particles in the atmosphere are classified as either cloud or aerosol based on their composition and physical characteristics. Both clouds and aerosols are crucial in various environmental processes, such as the global radiation budget and the hydrological cycle (Ramanathan et al., 1989). Still, they both remain to be a significant source of uncertainty in future climate projections. Indeed, the Sixth Assessment Report of the Intergovernmental Panel on Climate Change (IPCC) clearly states that predictions on how clouds will change in a warmer climate have been one of the biggest challenges in climate science (Masson-Delmotte et al., 2021).

Atmospheric aerosols are composed by small solid and/or liquid particles (0.01–100 μm), excluding hydrometeors, such as cloud droplets or precipitation (Wallace et al., 2006). The smaller aerosols (0.01–0.1 μm) are crucial in cloud formation processes as they can activate as cloud condensation nuclei (CCN) allowing the condensation of water vapour into cloud droplets or crystals (Lenoble, 1993). An increase in the number of CCN caused by anthropogenic aerosols may increase cloud reflectivity (Twomey, 1974), extend cloud lifetime (Albrecht, 1989), reduce drizzle or precipitation (Twohy et al., 2009), and change the cloud water content, affecting the cloud radiative forcing. Rosenfeld et al. (2014) also indicated that the evaporation of smaller droplets could enhance the mixing of unsaturated air into the

---

cloud, further enhancing evaporation processes. Therefore, aerosols can influence the radiation budget both directly, by scattering and absorption processes, and indirectly, by interacting and thus modifying cloud properties (Iqbal, 1983). In the shortwave band, aerosols scatter direct solar radiation, leading to more diffuse radiation. As a result, less solar radiation usually reaches the surface, causing localized cooling that could spread regionally and vertically through atmospheric circulation and mixing processes. In addition, radiation absorption results in the heating of the aerosol layer. The cooling-warming balance is determined by aerosol properties and environmental conditions. Despite the remaining uncertainties (e.g. in black carbon amounts, Wang et al., 2016), most studies agree that the overall aerosol radiative effect is to cool the planet (Masson-Delmotte et al., 2021).

Similarly, clouds induce different effects on radiation depending on their dimensions, opacities, and other properties, such as liquid water (or ice) content, and droplet (or crystal) size distribution. For instance, high wispy cirriform clouds, mainly composed of ice, generally have a net warming effect. Due to their thinness, sunlight can pass through them and warm the Earth's surface. Furthermore, this type of clouds absorbs more infrared radiation emitted by the Earth than they emit upward as they are colder than the surface, thereby warming the atmosphere. In contrast, low thick stratiform clouds tend to induce a net cooling effect. Composed primarily of water droplets, these clouds reflect back to space part of the sun's shortwave radiation, hence cooling the Earth's surface. Additionally, their relatively warm tops allow much of the infrared radiation received from the Earth to be radiated upwards (Ahrens, 2009).

Scientists studying the interactions between clouds and aerosols have commonly distinguished between cloudy and cloudless (yet containing aerosols) conditions in the atmosphere. However, this binary classification is not always well defined, as a gradual change in particle suspension characteristics from a cloudy to a non-saturated atmosphere could exist. For this reason, some studies argue the convenience of treating this phenomenon as a continuum between clouds and aerosols (Koren et al., 2007; Várnai and Marshak, 2009; Calbó et al., 2024). This is known as the "transition zone" or "twilight zone", which sometimes may be the result of turbulent mixing of clouds with non-saturated air (Wen and Marshak, 2022). In the current study, these intermediate conditions will be referred to as the *Transition Zone* (TZ). The TZ comprises all the aggregates of suspended particles in the atmosphere that cannot be clearly identified as cloud or aerosol. These suspensions include hydrated aerosol, haze, or forming/evaporating cloud fragments, that are often ignored by cloud-cloudless distinction methodologies (Koren et al., 2007).

Diverse processes take place within the TZ, such as the swelling and hydration of aerosol particles (Fuchs and Cermak, 2015; Schwarz et al., 2017; Murray et al., 2021), and the reduction in the size of cloud droplets (Wen and Marshak, 2022). These changes affect various parameters with the distance from the known cloud boundary, such as liquid water content (Simpkins, 2018), reflectance/emittance (Koren et al., 2008), relative humidity (Twohy et al., 2009), and precipitable water vapour (Wen and Marshak, 2022). Also, González and Calbó (2020) showed a rapid variation of optical depth, as well as rapid changes in its spectral pattern, before and after cloud detection.

Research on the TZ can be categorized into three main groups:

(I) Studies that aim to establish the TZ importance in the radiative balance. There are several noticeable studies within this category, including woks such as Charlson et al. (2007) and Koren et al. (2007), who advocate for a continuum of situations between clouds and cloud-free air. As already mentioned, it is important to consider this continuum, as excluding TZ aggregates to avoid the associated remote sensing uncertainties or including them despite the uncertainties, may lead to underestimated or overestimated aerosol optical depth, therefore biasing the study towards weaker or stronger radiative effects (Várnai and Marshak, 2011).

Other notable studies are those of Jahani et al. (2022) and Eytan et al. (2020), who aimed to represent the radiative effects of TZ suspensions. Both researchers combined satellite observations of outgoing longwave radiation with various other methodologies that estimate the fluxes in a cloud-free and aerosol-free atmosphere.

(II) Studies that aim to estimate the radiative effects in the longwave and shortwave spectral bands: The TZ affects radiation fluxes, which has been studied in the longwave (Eytan et al., 2020; Jahani et al., 2020), the shortwave (Jahani et al., 2019), and both spectral bands (Sola et al., 2024). These studies conclude that the actual effects of the TZ should be considered when parametrizing radiative transfer within weather and climate models, as they currently treat cloud and aerosols separately, not taking into consideration the TZ continuum.

(III) Studies that aim to estimate the extension or frequency of TZ conditions. Regarding TZ spatial coverage, Várnai and Marshak (2011) revealed the ubiquitous presence of TZ conditions over all oceans and extending up to 15 km away from the known clouds. Also, Twohy et al. (2009) estimated that the TZ affects >50% of the free atmosphere, highlighting its relevance in atmospheric processes. In order to estimate the TZ frequency of occurrence, Calbó et al. (2017) used three cloud observing systems (sky camera images, broadband solar radiation measurements, and spectral measurements) at two sites (Girona, Spain; and Boulder, Co, USA). Their findings revealed that, at least 10% of the temporal period analysed, "*the extension of scattered or broken cloud into cloud-free areas is problematic to establish and depends on where the limit is established between cloud and aerosol*". More recently, González et al. (2023) used downwelling longwave radiation from pyrgeometer measurements with the aim of estimating TZ situations for both daytime and nighttime periods and found that 10–15% of the observations could be attributed to the TZ.

The current research aims to build upon the third group of studies by incorporating ceilometer backscatter observations. Automatic Low-Power LiDAR and Ceilometers (ALC) are active instruments that emit brief laser-generated light pulses into the atmosphere and measure the backscatter signal reflected by suspended particles (Münkel et al., 2007). The backscatter profile (i.e. backscatter as a function of altitude) can be retrieved from the time delay between the emission and detection of the laser pulse. Originally ALC were developed for cloud base height (CBH) detection from the backscatter profile, but they have proven to be versatile instruments: the resulting backscatter profiles can be further processed to provide information on rainfall (Rogers et al., 1997), fog formation and dissipation (Haeffelin et al., 2010, 2016), aerosols within the atmospheric boundary layer (ABL) (Kotthaus and Grimmond, 2018), the ABL height (Kotthaus et al., 2020), detection of elevated layers of Saharan dust and biomass burning particles (Harrison et al., 2018), volcanic ash (Bedoya-Velásquez et al., 2021; Diémoz et al., 2022), and even drizzle properties by combining information with cloud radar data (O'Connor et al., 2005). Furthermore, ALC offer several advantages over other LiDAR, such as Raman or multiwavelength LiDARs. For example, ALC are more cost-effective and are designed for continuous measurements, enabling the generation of large datasets with high statistical significance (Marcos et al., 2018). While traditionally ALC have been deployed at airports for aviation purposes, they have also been used by national meteorological services, weather stations, research on extreme climates, and long-term campaigns (Wiegner et al., 2014; Kotthaus et al., 2016). These advantages have led to the creation of dedicated networks and programs focused on using ceilometers for atmospheric research. Some examples are the *E*-profile programme within the European Meteorological Services Network (EUMETNET), the Cloudnet project operated by the Aerosol Clouds and Trace Gases Research Infrastructure (ACTRIS), or the Aerosol LiDAR Ceilometer Network (ALICENET; Bellini et al., 2024). Specifically, the Cloudnet project aims to provide a systematic evaluation of clouds in forecast and climate models by contrasting the model output with ground-based measurements of vertical profiles of cloud properties (Illingworth et al., 2007).

Several methodologies have been developed to process ceilometer

data. The resulting algorithms can be categorized into two main groups. The first group provides information about the particles within the boundary layer and lower atmosphere: STRATfinder (Kotthaus et al., 2020), CABAM (Kotthaus et al., 2020), KABL (Rieutord et al., 2021), among others. The second group is designed for cloud detection: Cloudnet (Illingworth et al., 2007; Tukiainen et al., 2020), Polar Threshold (PT) (Van Tricht et al., 2014), Temporal Height Tracking (THT) (Martucci et al., 2010), ALCF 1.0 (Kuma et al., 2021), among others.

Considering all these previous studies, the goal of the present research is to determine the TZ frequency of occurrence using ground-based ceilometer observations processed by the open-source LiDAR scheme of the Cloudnet algorithm. This methodology will provide information about the vertical distribution of clouds, aerosols, and TZ conditions.

2. Methodology

To determine TZ conditions, we rely on cloud detection algorithms, following a similar strategy of Calbó et al. (2017) or González et al. (2023). More specifically, we consider as TZ situations all those cases in which there is a shift in cloud detection when employing different values for the thresholds applied to separate between cloudy and cloudless situations —the various thresholds used and the way they were determined will be discussed in Section 3b—. Indeed, most, if not all, cloud detection algorithms in any instrument (including ceilometers) require at some point an ad-hoc threshold for the separation. Determining what is classified as a cloud or cloud-free from a specific threshold may be quite controversial, and uncertain, particularly when deciding the exact value of that threshold. The applied scheme allows us to evaluate the occurrence of transition conditions, by distinguishing situations with more relaxed and stricter threshold values in the cloud detection algorithm applied to retrieved ceilometer backscatter profiles.

2.1. Profile retrieval

This work is based on the observations (retrieved backscattering profiles) from a Vaisala ceilometer model CL31 operating at the meteorological and radiometric station of the University of Girona (41.962° N, 2.829° E, 115 m a.s.l.). This is located next to the urban area of Girona (about 103,000 inhabitants by 2022), between the Mediterranean coast and the Pyrenees in a mainly flat area. Due to its location, the aerosol load above the site may contain some rural and oceanic particles, as well as urban (anthropogenic) aerosols. In addition, sometimes, and particularly in summer, the site is under the influence of Saharan dust intrusions and may also receive smoke plumes from wildfires (Sanchez-Romero et al., 2016). The average annual cloudiness is about 50%, with a strong seasonality that shows a clear minimum in summer (about 40% of cloud cover) (Calbó and Sanchez-Lorenzo, 2009).

The CL31 ceilometer located at Girona has been providing measurements on a vertical range 0–7.7 km, with 10 m resolution, since 2007. It is equipped with a CLE311 + CLR311 receiver (CLR) and engine board (CLE) and works under the firmware version 1.57. The laser source used by the CL31 is an Indium Gallium Arsenide (InGaAs) diode laser which emits 110 ns-long pulses at 910 ± 10 nm wavelength (at 25 °C) with a repetition rate of 10.0 kHz. According to the manufacturer, the pulses have a nominal energy of 1.2 μJ and are emitted by a transmitter with a half-angle beam divergence of 0.4 mrad × 0.7 mrad. The backscattered light is received and redirected to an optical interference filter with a typical centre wavelength of 915 nm and a 50% pass band of 36 nm. After the interference filter, the light reaches the silicon avalanche photodiode (APD) detector, which has a surface diameter of 0.5 mm, and a field-of-view divergence of ±0.83 mrad (Vaisala Ceilometer CL31 User's Guide).

In this work, about 1,9 million profiles retrieved during the year 2022, with a period of 16 s, have been analysed.

2.2. Profile treatment

The cloud detection algorithms used in this work are the Python package Cloudnetpy (Tukiainen et al., 2020) which implements the Cloudnet processing scheme (Illingworth et al., 2007), and the ceilometer manufacturer algorithm from Vaisala company. The limitation of the manufacturer algorithm is that neither the algorithm nor the thresholds used are published and cannot be changed (Kotthaus et al., 2016). However, given the extensive use of Vaisala ceilometers, the information resulting from that algorithm is commonly applied (e.g. Costa-Surós et al., 2013). Hence, in this study it is used as a reference for cloud detection. In contrast to Vaisala's algorithm and other ceilometer cloud detection algorithms and methodologies reviewed (i.e. Temporal Height-Tracking, THT, Martucci et al., 2010; Polar Threshold, PT, algorithm, Van Tricht et al., 2014; ALCF 1.0, Kuma et al., 2021; among others), Cloudnetpy stands out as an open-source, published, and highly cited algorithm. It not only allows the detection of clear-cloudy conditions, but also to classify the detected features between clouds and aerosols. It includes tests, documentation, and a user-friendly interface that the research community can use to further develop the existing methods and to create new products. Cloudnet processing scheme treats and combines information from LiDAR, cloud radar, microwave radiometer and numerical weather prediction models to retrieve diverse atmospheric conditions: rain drops, ice particles, melting ice particles, liquid droplets, supercooled liquid droplets, drizzle drops, insects and aerosol particles (Tukiainen et al., 2020). However, in the present study only the Cloudnetpy LiDAR scripts are used to treat only the ALC backscatter profiles.

Specifically, the function *ceilo2nc* in Cloudnetpy was used to retrieve the Signal-to-Noise Ratio (SNR) screened backscatter. This function can read several raw ceilometer files (including Vaisala CL31 files) and convert them into a Cloudnet Level 1b netCDF file. The resulting file contains three variants of the attenuated backscatter: the raw backscatter (β_{raw}), the SNR screened backscatter (β), and the SNR-screened backscatter with smoothed weak background (β_{smooth}).

To begin, the function establishes some parameters as the site information (the site name, altitude, calibration factor, if it is range corrected, etc.), and the Signal-to-Noise Ratio threshold (SNRth) is set. The SNRth establishes how much of the background noise is removed, where higher SNRth values are more restrictive and lower values are more relaxed (the predefined, default SNRth is set to 5). Function *ceilo2nc* englobes various embedded functions, but only the retrieval of the β variable is explained, as it is the only variable used for cloud detection in the present study. β is calculated using the function *calc_screened_product* that screens the noise from the backscatter variable calling the function *screen_data*. *Screen_data* involves the following steps:

- **Background noise calculation.** The background noise is estimated by taking a subset of the top gates (i.e. levels) of each backscatter profile. This estimation involves calculating the square root of the variance of each subset. After that, a function (*_adjust_noise*) checks whether the estimated background noise is lower than a defined noise threshold. If so, it replaces those values with a defined minimum value (1×10^{-9} m^{-1} sr^{-1}).
- **Filter negative and low values above consecutive negatives.** The function *mask_low_values_above_consequent_negatives* identifies profiles that have over 5 consecutive negative backscatter values. It uses the first 100 gate values from the 5th gate (in CL31 corresponds from 50 m to 1050 m). After that, the function removes from the processing the subsequent backscatter values below a given threshold, in this case 8×10^{-6} m^{-1} sr^{-1} (these values are called "masked" values hereinafter) and returns an array indicating which profiles contain negative values. If the *filter_negative* is set to True, the negative values are set to a small positive value (1×10^{-12} m^{-1} sr^{-1}).
- **Filter saturated profiles.** The function *_find_fog_profiles* finds saturated profiles (e.g. thick fog, thick clouds) from β_{raw}, based on a

combination of signal sum and variance thresholds in the first 20 gates (in CL31 corresponds to the first 200 m) from each profile. Profiles that either exceed the signal sum threshold (predefined value is $1 \times 10^{-3}\,\mathrm{m}^{-1}\,\mathrm{sr}^{-1}$) or have lower variance than the variance threshold (predefined value is $1 \times 10^{-15}\,\mathrm{m}^{-1}\,\mathrm{sr}^{-1}$) are considered as saturated profiles. In the saturated profiles found, the function _clean_fog_profiles_ detects the values that are above the peak (maximum backscatter) and are smaller than a threshold value (the predefined value is $2 \times 10^{-6}\,\mathrm{m}^{-1}\,\mathrm{sr}^{-1}$). If the _filter_fog_ is set to "True", those values are set to a small positive value ($1 \times 10^{-12}\,\mathrm{m}^{-1}\,\mathrm{sr}^{-1}$).

- **Remove values with high SNR.** The function _filter_snr_ masks values with higher SNR than a given SNRth value, as mentioned above. SNR values are calculated for each point, where each backscatter value is divided by the calculated background noise.

- **Range correction calculation**. The range corrected signal (RCS) is defined as "the background corrected signal, additionally corrected for the $1/r^2$ dependency" (Mattis and Wagner, 2014), being r the range (distance from the ceilometer). In this regard, the _calc_range_corrected_ function takes the range as a factor for some values. If the parameter _range_corrected_ is set to "False", it takes the first 2400 m, otherwise, it takes all ranges.

Once the β variable is retrieved, cloud detection is estimated based on a backscatter threshold (Bth) value (in the code referred to as _cloud_limit_). In other words, Bth determines whether a backscatter value can be considered as cloud or not. The predefined value for cloud detection in the original Cloudnet scheme is Bth $= 20 \times 10^{-6}\,\mathrm{m}^{-1}\,\mathrm{sr}^{-1}$ (Tuononen et al., 2019).

Additional details of the Cloudnetpy code and methodology are provided by Tukiainen et al. (2020), Illingworth et al. (2007) and in the Cloudnetpy documentation (accessible at the website https://cloudne tpy.readthedocs.io/en/latest/).

The data provided by the CL31 ceilometer is already corrected for overlap, atmospheric background signal and range. However, the system software does not subtract the electronic background from the total signal (O'Connor et al., 2004). Usually, this electronic background is several orders of magnitude weaker than the signal backscattered by clouds and can be disregarded for studies focused on cloud detection (Marcos, 2017). Moreover, as the evaluation of absolute calibration techniques is beyond the scope of this study, the calibration factor is neglected (i.e., calibration factor is set to 1). Nonetheless, the uncertainties in the calibration are considered within the magnitude of the Bth, as the calibration factor multiplies the backscatter values.

3. Results and discussion

3.1. Cloud detection

This section assesses the accuracy of the Cloudnetpy algorithm for its cloud detection and cloud occurrence estimation. A set of conditions are applied to the algorithm to determine the predefined situation: Bth $= 20 \times 10^{-6}\,\mathrm{m}^{-1}\,\mathrm{sr}^{-1}$, SNRth $= 5$, _calibration factor_ $= 1$. A comparative analysis between this and the proprietary Vaisala algorithms was conducted by contrasting cloud detection for each profile and by comparing the hourly Cloud Occurrence (CO). The CO is the ratio of cloud hits to the total number of profiles analysed within a given time period (1 h in our case). In this context, a "hit" refers to a backscatter profile containing at least one cloud detection. The CO is usually considered a rough estimator of the cloud cover (CC) which is defined as the portion of the sky cover that is attributed to clouds.

First, the differences in testing each profile with the two algorithms were analysed. The results show that the two algorithms agree in 94.3% of the cases, as 28.7% profiles exhibited cloud detection hits while 65.6% were identified as cloud-free. For the remaining 5.7% of profiles, cloud detection depended on the algorithm used, including 3.2%

missing hits (detected by Vaisala and not by Cloudnetpy), and 2.5% false detections (detected by Cloudnetpy and not by Vaisala). Through visual observations of the backscatter profiles, we perceived that missing hits appear to be related to the presence of high clouds, whereas Cloudnet detects more low-level features than Vaisala.

Regarding the hourly CO obtained by the two algorithms, a comparison is shown in Fig. 1. In an ideal situation where the two algorithms perfectly agree, the points would align along the diagonal, referred to as the identity line between the two estimations. Although it is quite apparent that most points cluster along the identity line, further detail about the differences between the algorithms is given in Fig. 2, which shows the histograms of the hourly CO in bins of 5%. Most of the hourly CO exhibit values of 0–5% (>4000 profiles), and 96–100% (>1000 profiles) for both Cloudnetpy and Vaisala estimations. Therefore, to provide a clearer contrast, Fig. 2b excludes values that are exactly 0% or 100% in CO (so the first bin in Fig. 2b contains the range 1–5% and the last bin, the range 96–99% of CO). Then, the distribution reveals a U-shape pattern, with greater frequency for low and high occurrence ranges (<20% and > 75%). Both algorithms show similar distributions across all CO bins. However, Cloudnet presents slightly higher values for CO $= 100\%$, and also in the range 1–25%, while lower values are observed for CO $= 0\%$, and in the range 80–99%. Therefore, it is difficult to generalize a tendency of over or underestimation, but the average CO for the whole dataset is 31.9% from Vaisala and 31.2% by applying Cloudnetpy. These values are clearly lower than climatic mean of cloud cover, which may be due to some missing high clouds (as the range of CL31 ceilometer reaches only up to 7.7 km) and due to the limited time period (1 year) analysed in the present study (so with no climatic representativeness). As a conclusion of the comparison, Cloudnetpy algorithm with the default thresholds (Bth $= 20 \times 10^{-6}\,\mathrm{m}^{-1}\,\mathrm{sr}^{-1}$, SNRth $= 5$) accurately reproduces the cloud detection as performed by the Vaisala algorithm.

3.2. Transition zone

Having established that Bth $= 20 \times 10^{-6}\,\mathrm{m}^{-1}\,\mathrm{sr}^{-1}$ and SNRth $= 5$ result in a good estimate for cloud detection, we investigated the impact of varying each threshold. As an example of the assessment, the backscatter values with their classification (cloud/cloud-free) acquired in a particular day, 27th September 2022, are shown in Fig. 3.

First, Fig. 3a shows conditions throughout the 27th September 2022 as recorded by a number of sky hemispheric images, taken with a SONA
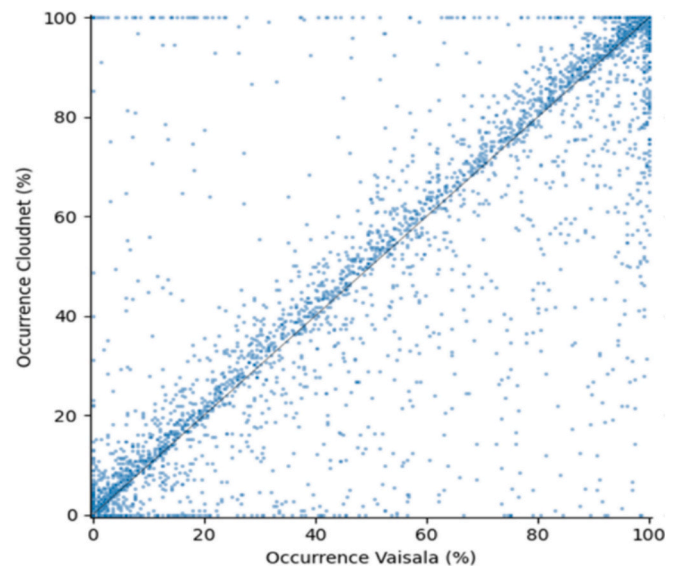

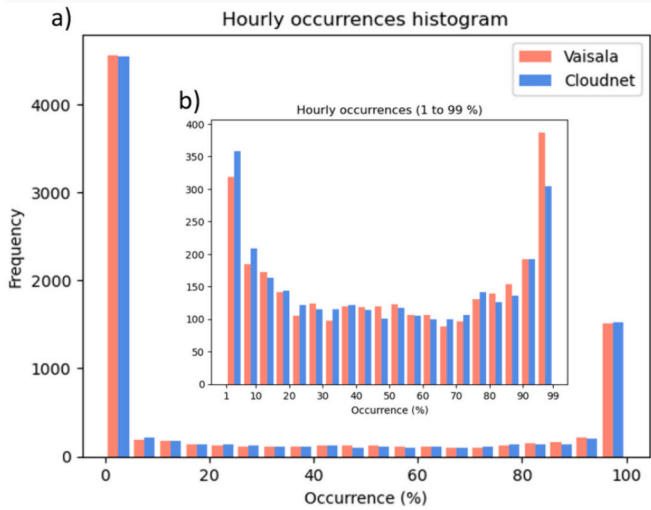**Fig. 1.** Cloudnetpy versus Vaisala hourly cloud occurrences. Identity line is also shown.

Fig. 2. Distribution (in 5% bins) of the absolute frequency of CO, as retrieved by the Cloudnetpy and the Vaisala algorithms. a) All cases; b) Excluding cases with 0 or 100% CO.

(from Sieltec Canarias) camera. During the early morning, the atmospheric conditions exhibited a predominantly cloudless sky, although a few middle clouds appeared at around 4 UTC (image not shown). From sunrise to 9 UTC high wispy *Cirrus* clouds were detected (some of them still visible in the SONA image for 10 UTC), and as the morning progressed into the afternoon (9–15 UTC), scattered low-level clouds kept appearing on the site. Towards the evening (from 18 UTC onwards, see image for 20 UTC), broken clouds appeared, contributing to the overall cloud coverage. Finally, the SONA image at 23:59 UTC shows again an almost cloudless sky.

In the evolutions shown in Fig. 3b-3d, values of SNR and B higher than the corresponding SNRth and Bth thresholds (i.e., cloudy values) are represented in red, and cases with values lower than the thresholds but not masked out by the Cloudnetpy algorithm are shown in light red (i.e., atmospheric aerosol, haze, etc.). Additionally, values masked out by the Cloudnetpy algorithm are depicted in white; such values are not considered as valid in the rest of the analysis, and would correspond to very small or negative values, saturated profiles, high background noise, etc. Specifically, Fig. 3b correspond to applying the default thresholds; Fig. 3c shows the effect of lowering SNRth to 2.5; while Fig. 3d shows the effect of lowering Bth to 1×10^{-6} m^{-1} sr^{-1}. On the top of each panel (Fig. 3b-3d), hits (that is, the presence of at least one cloudy value in a profile) are shown in a coloured band. Cloud hits with default thresholds are shown in blue, no hits in white, and new hits obtained by lowering the threshold values are highlighted in orange.

For this particular day, the cloudy values for the default thresholds represent 0.73% out of all backscatter values, and a CO (i.e., hits divided by the total number of profiles) of 48.7% (Fig. 3b). For the lowered SNRth, high cloud detections are enhanced, but also more noisy values
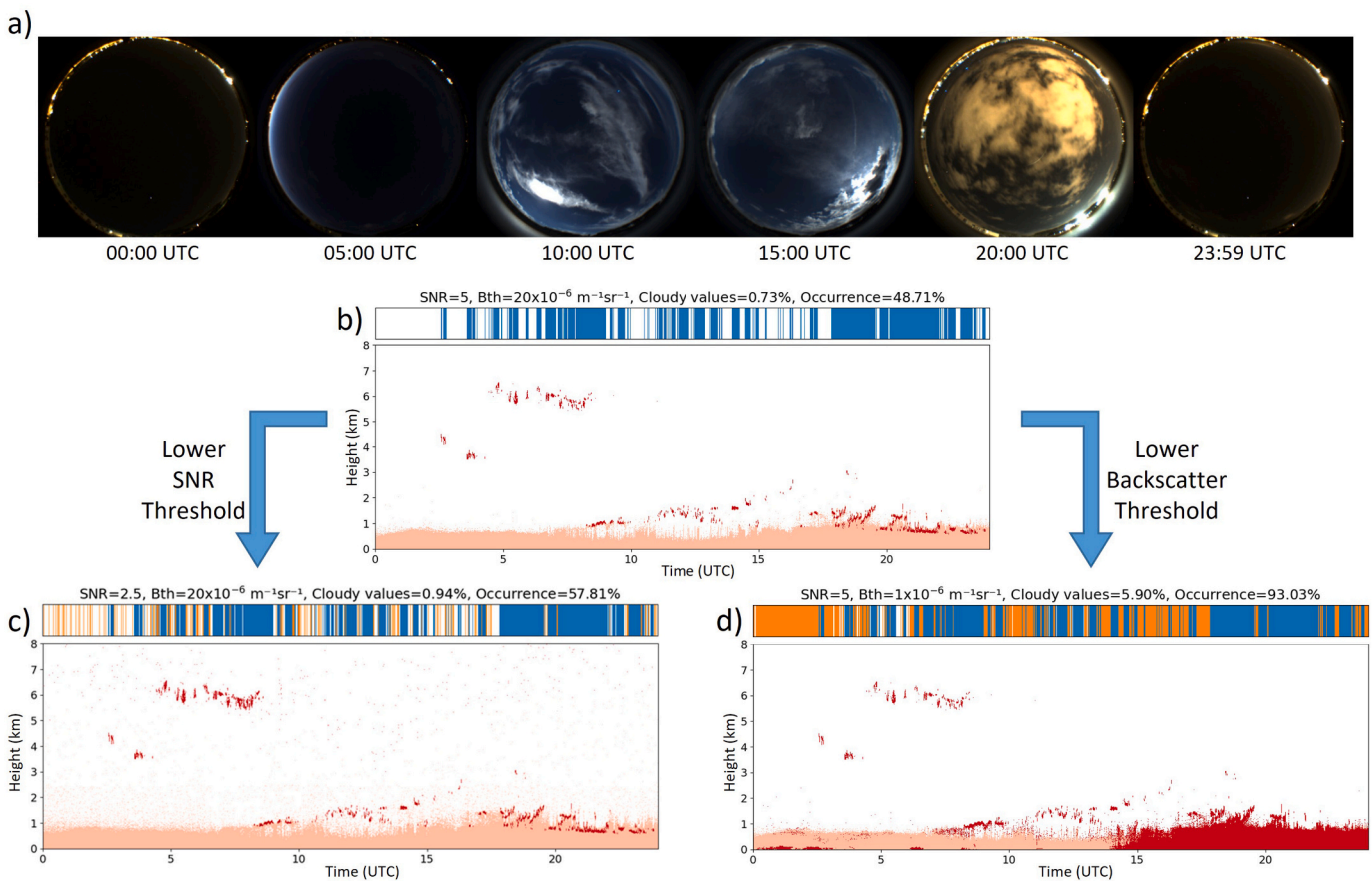

Fig. 3. Impact of SNRth and Bth on cloud detection for 27th September 2022. a) Camera SONA images through the day; b) Cloud detections with the predefined values (SNRth = 5 and Bth = 20×10^{-6} m^{-1} sr^{-1}); c) Cloud detections with a very relaxed SNRth (SNRth = 2.5); d) Cloud detections with a very relaxed backscatter threshold value (Bth = 1×10^{-6} m^{-1} sr^{-1}). Values higher than SNRth and Bth thresholds are depicted in red, lower values are in light-red, and values masked by the algorithm (i.e. noise) are in white. Cloud hits for each profile are shown in top of each panel. In blue, detections with the predefined threshold values; in orange, new detections as a result of lowering the threshold values; in white, profiles with any detection. The percentage of cloudy values and cloudy occurrence for each situation is also shown. (For interpretation of the references to colour in this figure legend, the reader is referred to the web version of this article.)

across all height ranges are introduced (Fig. 3c). For that situation, cloudy values represent the 0.94%, and CO is 57.8%. Finally, for the lowered Bth, more features are detected near low-level clouds (Fig. 3d). Thus, in this situation the cloudy values reach 5.90% of all backscatter values and CO grows up to 93.0%.

A direct comparison between the images and the cloud detections from the ceilometer observations does not make much sense, as ceilometers can only detect the vertical structure directly above the instrument. Another limitation is the low sensitivity for detecting high clouds that may bias the analysis (Román et al., 2017). Nevertheless, cloud detections, and in particular profile hits, match in a general sense what can be observed in the images, at least for the case of the default thresholds; for the lowered thresholds, the number of detections appears to be excessive as compared to whole sky images.

Furthermore, we conducted a sensitivity analysis to assess more comprehensively the impact of the detection thresholds; this analysis is the basis to determine the occurrence of TZ conditions. First, we counted hits (profiles containing at least one backscatter value labelled as cloudy) depending on the combinations of threshold values (Bth and SNRth). This is shown in Fig. 4a, as a percentage of hits relative to the total number of profiles. Fig. 4a clearly shows that as the thresholds are relaxed, more hits are obtained. For example, in the bottom left corner (SNRth <3; Bth < 1×10^{-6} m^{-1} sr^{-1}) the thresholds are too relaxed that result in a lot of hits (close to 100%), which means that many noisy backscatter values are classified as cloudy. At the other end, in the right side of the figure, values of Bth > 200×10^{-6} m^{-1} sr^{-1} are too strict, and the number of hits falls down to <20%, so they are useless as cloud detection threshold, since these extremely high backscatter values likely correspond to very dense/big cloud droplets or precipitation. The percentage of hits obtained by all ranges of Bth with SNRth values set to 5 and 4 is depicted in Fig. 4b (that is, the frequencies corresponding to the blue and red dashed lines of Fig. 4a, respectively). Since SNRth = 4 is less strict than the default value (SNRth = 5), it gives more hits, which is particularly apparent for Bth between 0.5 and 20 ($\times 10^{-6}$ m^{-1} sr^{-1}). Both curves show a significant decrease in the number of hits for Bth between 1 and 4 ($\times 10^{-6}$ m^{-1} sr^{-1}) and from 100 to 1000 ($\times 10^{-6}$ m^{-1} sr^{-1}). As already mentioned, there is little variation for Bth < 0.7×10^{-6} m^{-1} sr^{-1} (as all profiles are identified as hits because the threshold is too relaxed), and also for Bth > 1000×10^{-6} m^{-1} sr^{-1} (as hardly any profile is identified as hit because the threshold is too strict). Curves present an additional "plateau" for values of Bth of around 10×10^{-6} m^{-1} sr^{-1}

which is precisely the region where some arbitrariness or subjectivity appears when choosing the adequate thresholds for cloud detection. In other words, the shift between cloud and cloud-free conditions is gradual, so the detection by a ceilometer depends quite critically on the thresholds used.

As mentioned above, we will assume that those profiles that show or do not show a hit depending on the thresholds used for cloud detection correspond to transition zone conditions over the site. The default values of SNRth = 5 and Bth = 20×10^{-6} m^{-1} sr^{-1} are considered as the strict set of thresholds, since with these values the result matches very well the cloud detection by the Vaisala algorithm. With these values, we obtain 31.2% of hits. For the relaxed situation, we take SNRth = 4 and Bth = 3×10^{-6} m^{-1} sr^{-1}, values that are in the limit of the "plateau" area. With these values, the number of hits reaches 40.5%. As the uncertainties in the calibration propagate through Bth values, we have checked two additional Bth values: 2×10^{-6} m^{-1} sr^{-1} and 4×10^{-6} m^{-1} sr^{-1} (thick orange lines in Fig. 4b). With these values, the number of hits is 36.6 and 51.2% respectively. Comparing the number of hits from the relaxed thresholds with that from the default (strict) thresholds, we conclude that TZ conditions represent about 9.3% [5.4–20%] of the total, where the number within brackets indicate the range of uncertainty related to the uncertainty derived both from the arbitrariness in the selection of thresholds and from not applying a calibration factor to backscatter values. A summary of the thresholds applied is shown in Table 1.

These results are similar to those of Calbó et al. (2017) or González et al. (2023), who found "at least 10%", and "10–15%" of TZ conditions in Girona, respectively. They are also comparable to other studies that analysed the TZ spatial coverture (e.g. Várnai and Marshak, 2011; Twohy et al., 2009). All these studies classify sky conditions as cloud,

Table 1
Thresholds used to detect cloud, transition zone and aerosol in backscatter profiles from ceilometer.

	SNRth	Bth ($\times10^{-6}$ m^{-1} sr^{-1})	Threshold tolerance
Cloudy	SNR > 5	β > 20	STRICT
	4 < SNR < 5	3 < β < 20	RELAXED
Transition zone	4 < SNR < 5	2 < β < 20	MORE RELAXED
	4 < SNR < 5	4 < β < 20	LESS RELAXED
Cloud-free (aerosol)	SNR < 4	β < 3	
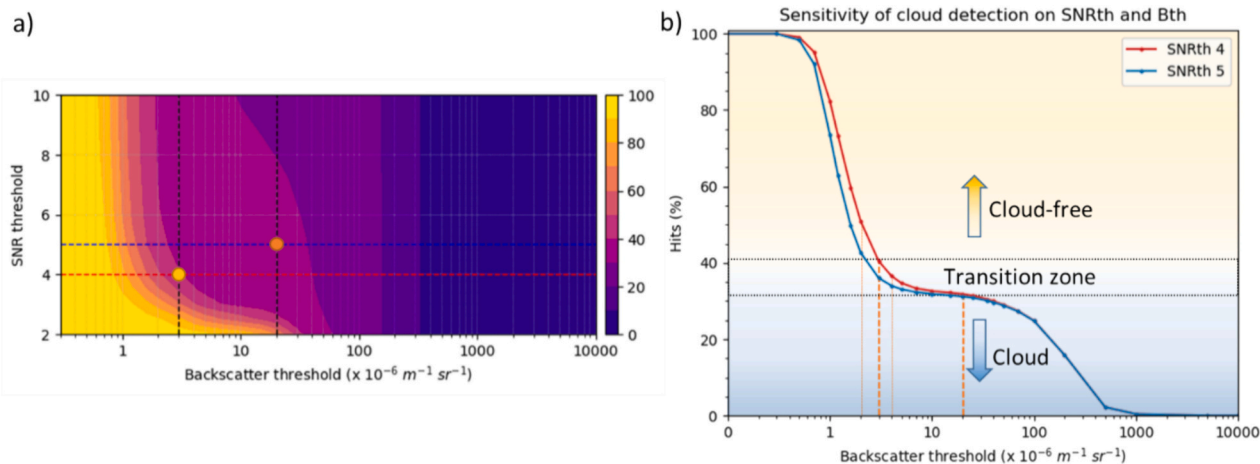
Fig. 4. Cloud detection on Bth and SNRth. a) Contour plot of the relative number of hits, that is a backscatter profile containing at least one cloud detection, depending on thresholds Bth and SNRth. Blue and red dashed lines correspond to SNRth = 5 and SNRth = 4, the lowest and highest thresholds used for TZ determination and represented in Fig. 4b. The orange dot is the exact position for the default (strict) thresholds (SNRth = 5 and Bth = 20×10^{-6} m^{-1} sr^{-1}), while the yellow dot corresponds to the relaxed thresholds (SNRth = 4 and Bth = 3×10^{-6} m^{-1} sr^{-1}); b) Relative number of hits for different Bth values. Dashed orange lines correspond to the set of thresholds used for characterising the TZ as described in Table 1. (For interpretation of the references to colour in this figure legend, the reader is referred to the web version of this article.)

TZ, or cloud-free (albeit containing aerosols), by considering the atmospheric conditions integrated in the whole column, as all methods applied rely on ground-based measurements or observations that are unable to provide any vertical structure. In contrast, ceilometers allow us to go further and analyse the backscatter signal along the vertical.

Before studying the vertical structure, however, we have analysed the effect of changing the thresholds on each backscatter value. Thus, Fig. 5 illustrates the number of cloudy values depending on Bth (and for the two values of SNRth above considered). This approach reveals an additional 103% [84–153%] of TZ values (from Bth = 3 [2—4] $\times 10^{-6}$ m^{-1} sr^{-1}; SNRth = 4) compared to the cloudy values (from Bth = 20 $\times 10^{-6}$ m^{-1} sr^{-1}; SNRth = 5), that is a number of TZ values similar to the number of the initial cloud categorization. These results for the volumetric view of the atmosphere suggest that the TZ may have a greater presence than initially estimated, as particle suspensions with characteristics of TZ conditions may be as ubiquitous as those suspensions corresponding to cloud conditions. Consequently, this justifies the need for a more exhaustive investigation of its vertical extension.

Therefore, having established the classification thresholds for each condition (cloud, transition zone, cloud-free —albeit containing aerosols—, see Table 1), we first applied them to the backscatter profiles of the case study analysed in Fig. 3. Indeed, Fig. 6 shows the results of such analysis, and it is observed that TZ conditions are detected mostly above, below, and around (in the temporal sense, which due to cloud movement, corresponds to spatial sense too) cloud features. This is especially obvious from 18 UTC to midnight. Given the interest of this period, Fig. 6b provides a detailed view of the ceilometer detections between 18:45 UTC and 20:30 UTC, and Fig. 6c shows the SONA images taken every 5 min between 19:15 UTC and 20:10 UTC. During this period, many cloud pockets were forming and dissipating, so the cloud cover above the station continuously changed. At the same time, the ceilometer profiles exhibited an almost constant layer of TZ detections below 800 m, and clouds appearing above it. Moreover, the raw backscatter profiles suggest that the TZ layer detected below 800 m during the evening could potentially correspond to humified aerosols (Fig. B1).

3.3. Detection distributions

The analysis of the vertical structure of the different conditions can be extended to all backscatter profiles included in the present study. Figs. 7 and 8 present the vertical and temporal distributions of the detected features, categorized as cloud, TZ, or aerosol based on the thresholds given in the previous section (Table 1) for the whole 2022 dataset. It should be noted that in these figures we are representing the counts of backscatter values, not of profiles; therefore, as we showed in Fig. 5, the amount of TZ detections is comparable to the number of cloudy values.

Aerosol suspensions are detected within the first 2000 m, especially below 1000 m. It should be noted that the number of aerosol detections reaches nearly 1.8 million at some low heights (Fig. 7). Regarding cloud detection, more cloudy values are observed at lower altitudes, with the number of detections gradually decreasing with height. Notably, very few clouds are detected above 7000 m, due to the ceilometer range of detection. As the ceilometer beam approaches this altitude, it might already be quite attenuated, thus underestimating cloud detections. Furthermore, as the beam is weaker, and there is more noise, Cloudnetpy masks (do not consider valid) low backscatter signals (i.e. potential TZ and aerosols) and only processes stronger signals that are categorized as clouds. Therefore, this contributes to underestimation of TZ and aerosols at high altitudes. The distribution of the TZ suspensions lies in between that of aerosol and that of clouds. Indeed, most TZ detections are found below 800 m (with a maximum frequency at very low levels), while between 800 and 2400 m, the number of detections progressively decreases. Beyond 2400 m and up to 7700 m, TZ conditions are still detected but in a lesser amount, specially over 4000 m.

The hourly evolution (Fig. 8) shows that in general there are more feature (cloud-TZ-aerosol) detections between 15 and 4 UTC (i.e., from evening to early morning) compared to 6–13 UTC (morning and early afternoon). This is particularly true for aerosol detections, which show a clear daily cycle with a minimum in the morning (7–12 UTC) and a maximum in the evening (18–19 UTC). Clouds and TZ exhibit a similar evolution with less detections in the morning (6–12 UTC) than in the afternoon-night periods (15–4 UTC). The number of cloudy values is slightly higher than TZ values at around noontime, while the opposite is true during evening and early night hours.

Fig. 9 shows the daily evolution of vertical distributions, which reveals differences between day and night. During night-time and early morning (20–9 UTC), clouds are found at all heights, but especially below 200 m, corresponding to foggy conditions, as also seen for instance by Haeffelin et al. (2016) and Toledo et al. (2021). In contrast, during daytime (10–19 UTC), a greater number of clouds are found between 200 m and 3000 m, probably as result of convective clouds (Fig. 9a and d). As far as aerosol detection is concerned, these values are concentrated below 1000 m height, and scarcely found higher than 2000 m (Fig. 9c and f). As expected, TZ distribution is somewhat in between the other two: it follows a similar pattern to clouds as most detections are found below 300 m during 18–6 UTC and under 3000 m between 13 and 18 UTC; while TZ conditions are hardly detected above 3000 m at any time (although there are some detections at all heights, like in the case of clouds). The high frequency of transition zone aggregates during nighttime and low altitudes suggests that these aggregates are the result of hydrated stages of aerosols. During nighttime, the surface and low altitude temperatures decrease, while the relative humidity increases, leading to more moisture, more humid aerosols, haze, and in some cases, fog and low clouds. Furthermore, the TZ aggregates found during daytime (e.g. around convective clouds, boundary layer clouds), may result from cloud-aerosol interactions, cloud formation, cloud edges, or thin clouds with low optical depths.

These annual height-hour distributions englobe a remarkable variability among seasons (see Fig. A1 presented in Annex A). Indeed, during colder seasons, such as autumn and winter, cloud and TZ detections are mainly localized below 200 m between 22 and 10 UTC, corresponding to fog or mist that could further develop into a layer of low stratus clouds. In summer, there are fewer clouds (and also fewer TZ) detections, and they are much more concentrated in afternoon hours, as a result of the daily evolution of convective clouds. In spring, there is a high variability in clouds found below 5000 m and TZ below 3000 m. Contrarily, the
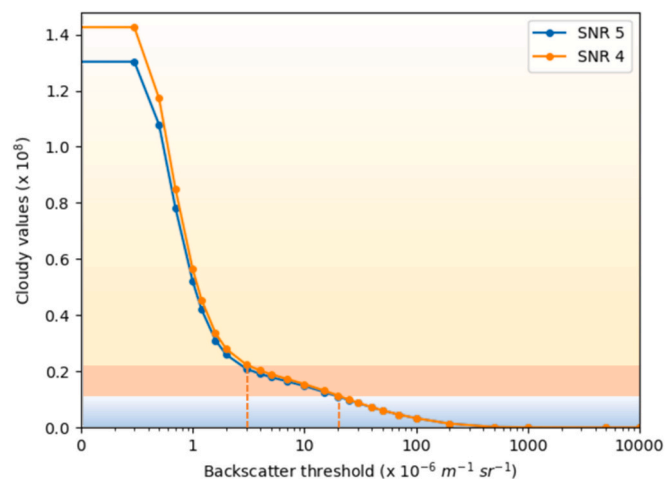

Fig. 5. Sensitivity of the number of cloudy values on Bth and SNRth. The background colours represent the suspensions from a cloudy to cloud-free atmosphere, with clouds (blue), TZ (orange) and cloud-free containing aerosol (yellow). The vertical orange dashed lines show the threshold used to determine the TZ. (For interpretation of the references to colour in this figure legend, the reader is referred to the web version of this article.)
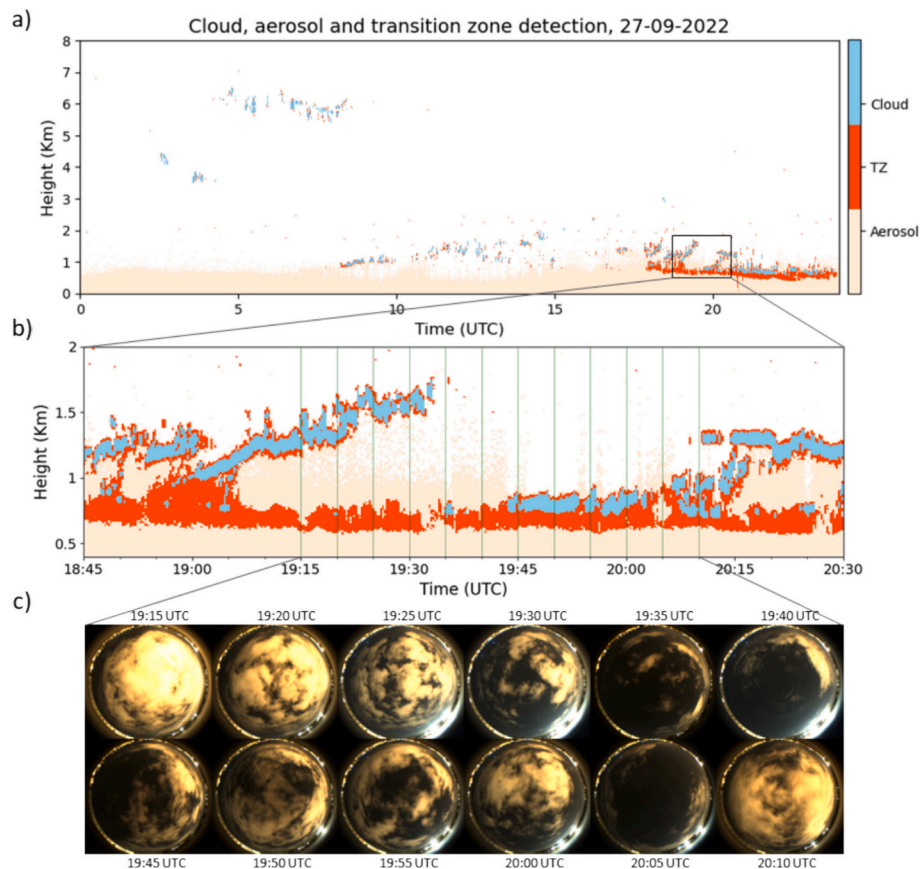
Fig. 6. An example of cloud, TZ and aerosol detections at Girona's radiometric station, on 27th September 2022. a) ALC detections throughout the day; b) Close up detections for 18:45–20:30 UTC; c) SONA images taken every 5 min between 19:15 UTC and 20:10 UTC.
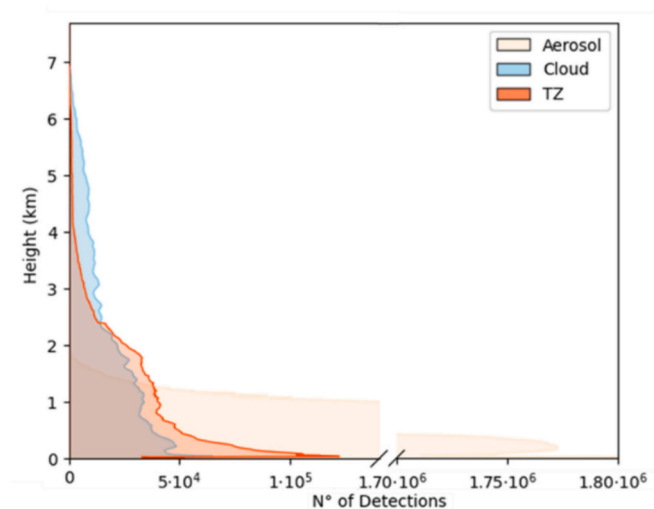

Fig. 7. Height distributions of cloud-TZ-aerosol detections for 2022. It should be noted that the brown colour is the result of superposition between the other three colours (orange, blue, beige). (For interpretation of the references to colour in this figure legend, the reader is referred to the web version of this article.)

Fig. 8. Hourly distributions of cloud-TZ-aerosol detections for 2022. As in Fig. 7, the brown colour is the result of superposition between the other three colours (orange, blue, beige). (For interpretation of the references to colour in this figure legend, the reader is referred to the web version of this article.)

distribution of aerosols does not vary much among the seasons.

4. Concluding remarks

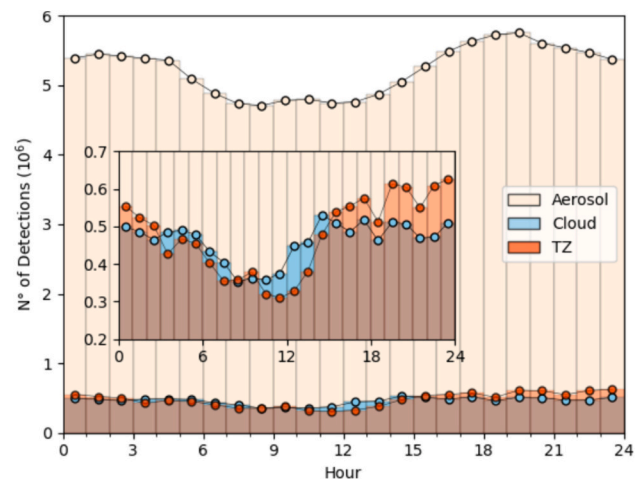The main objective of the present study has been to determine the frequency of transition zone situations by using observations from a ground-based LiDAR ceilometer, specifically a Vaisala CL31 ceilometer located at Girona, Spain. The underlying hypothesis is that establishing a specific threshold value to determine whether a backscatter value is classified as cloud or not is inherently challenging due to the cloud-aerosol continuum. We have based the study on processing the back-scatter values with the Cloudnet LiDAR algorithm (Cloudnetpy) which
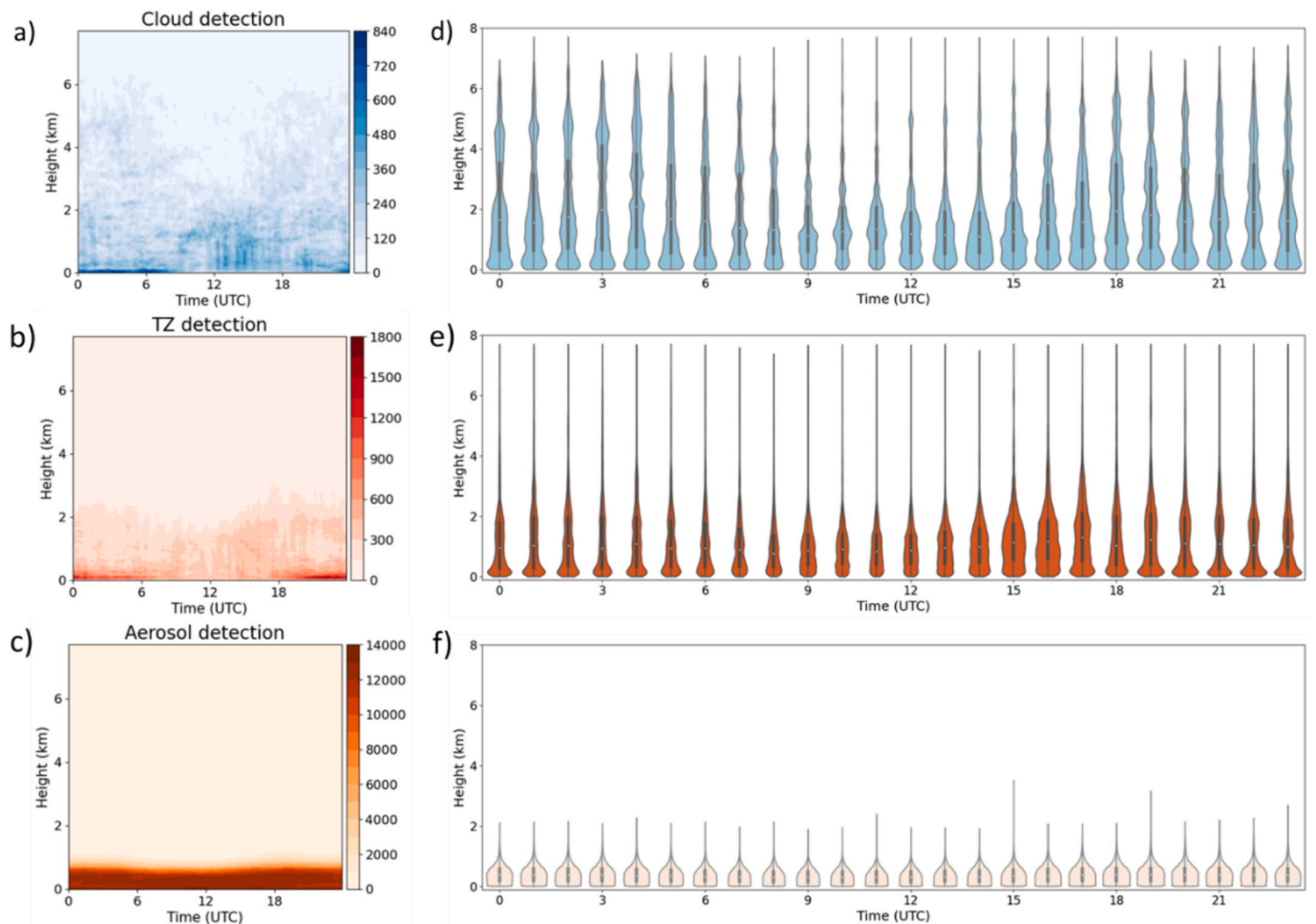
Fig. 9. Evolution of vertical distribution for cloud (a, d), TZ (b, e) and aerosol (c, f) detection, from the backscatter profiles retrieved at Girona in 2022. a) Cloud detection density; b) TZ detection density; c) Aerosol detection density; d) Vertical distribution of hourly cloud detections; e) Like d), but for TZ; f) Like d) but for aerosol.

has first been compared to the proprietary Vaisala algorithm. The analysis has been performed over a set of backscatter profiles retrieved every 16 s along the year 2022.

Even though the criteria of the two algorithms are not the same, there is a noticeable agreement between them. Using Cloudnet LiDAR processing scheme with the default thresholds of SNRth = 5 and Bth = 20×10^{-6} m^{-1} sr^{-1}, cloud detection (counting profiles with at least one cloudy value) is 94.3% in accordance with Vaisala algorithm. The main differences between the two methods are some missing hits (Vaisala seems to detect high clouds better), and some false detections (Cloud-netpy tends to detect more low-level features).

Since backscatter observations exhibit a gradual transition from clouds to cloud-free, and cloud detection is influenced by the thresholds used, we have defined transition zone conditions as those backscatter values that are not considered clouds by the default thresholds, but that are, in contrast, considered clouds by a "relaxed" set of thresholds (SNRth = 4 and Bth = 3×10^{-6} m^{-1} sr^{-1}). To account for the associated uncertainty, we also checked two other values for Bth (2×10^{-6} and 4×10^{-6} m^{-1} sr^{-1}). Within the whole set of backscatter values, we found as many TZ conditions as cloudy conditions (the number of TZ counts is 103% [84–153%] of cloudy counts), which emphasises the importance of the transition zone suspensions and of studying their vertical distribution. If we take a vertically integrated view (that is, we count the profiles that contain at least one TZ value but no cloudy values), the result is that TZ situations appear 9.3% [5.4–20%] of the time period analysed. This value is comparable, and similar to the estimations of TZ

frequency by Calbó et al. (2017) and González et al. (2023) using other kind of observations at the same site (Girona's radiometric station), but a similar methodology built upon the uncertainty of applied thresholds. Thus, Calbó et al. (2017) used sky camera images, broadband solar radiation measurements, and spectral measurements, finding at least 10% of the temporal period attributed to the TZ, whereas González et al. (2023) used downwelling longwave radiation from pyrgeometer measurements, finding that 10–15% of the observations could be attributed to the TZ.

Unlike the latter studies, the use of ceilometer backscatter data allows the study of the vertical distribution of cloud, transition zone and aerosol suspensions. It should be noted that we have defined aerosols as those backscatter values that are not filtered out or masked by the first steps of the algorithm, but which are not labelled as cloud even when applying the "relaxed" set of thresholds. With these definitions, aerosols were mainly observed below 1000 m, while clouds were detected at all heights with a greater occurrence at low altitudes. The distribution of TZ suspensions lies between that of aerosol and clouds, but its pattern is more like clouds, with more TZ detections at lowest levels (< 300 m) and fewer detections above 3000 m. From the temporal point of view, greater detection rates were observed during the evening and night periods, whereas the morning hours (e.g. 5–12 UTC) exhibited fewer detections. Such results agree for instance with two very recent studies. Yang et al. (2024) states that resolving droplet formation under atmospheric cloud conditions is challenging, which impedes understanding cloud-aerosol interactions. By using a single-photon lidar their results

also show that "*the air-cloud interface is not a perfect boundary but rather a transition zone where the transformation of aerosol particles into cloud droplets occur. The observed distributions of first-arriving photons within the transition zone reflect vertical development of a cloud, including droplet activation and condensational growth.*" Khain et al. (2024) studied the dynamics and microphysics of cumulus clouds, with special attention to the mechanisms of cloud-surrounding interactions. They also show that turbulence is responsible for forming "*an interface zone between the cloud and the surrounding air*" (in the present paper referred to as TZ).

It is important to notice that occasionally TZ aggregates are found without any nearby clouds, both spatially and temporally. As a result, the TZ encompasses not only "the gradual transition from clouds to cloud-free" conditions but also suspended aggregates with borderline properties, like haze, that may not necessarily be located near cloud fragments.

The results of this research highlight the noticeable frequency and vertical spatial extension of TZ situations, emphasizing the importance of further investigation in this area. Regardless of the methods and instruments used for cloud detection (either visual observations or sophisticated sensors), there are always conditions under which clouds are difficult to distinguish. Furthermore, sensors such as cameras, lidars, radars and other narrow-band radiometers may operate at different wavelengths than visible (infrared, microwaves, etc.) and from various platforms (ground-based, satellites, aircraft). These instruments, however, do not necessarily detect the same as a human observer would see, which further complicates the traditional binary categorization of atmospheric particle suspensions into cloud and cloud-free states (Calbó et al., 2024). These suspended aggregates that cannot be clearly classified as cloud or cloud-free (but containing aerosol load) have a significant impact on the radiative balance (in the shortwave and longwave) and should not be ignored. Excluding TZ aggregates to avoid the associated uncertainties, or including them despite the uncertainties, may lead to underestimated or overestimated aerosol optical depths, therefore biasing the study towards weaker or stronger radiative effects (Várnai and Marshak, 2011). This calls for a more comprehensive approach, as clouds are parametrised but still not resolved in climate models, needing more precise observations and presenting challenges in

their parametrisations (Khain et al., 2024; Yano et al., 2018). To improve such parametrisations (in particular, the radiative effects) a suggestion could be to either include an intermediate phase between clouds and aerosols or treat all suspended particles in the atmosphere as a continuum of states. Such approach could eventually improve the accuracy of atmospheric models and forecasts, particularly by better representing the radiative effects of this continuum of conditions (Calbó et al., 2024).

CRediT authorship contribution statement

Declaration of competing interest

The authors declare that they have no known competing financial interests or personal relationships that could have appeared to influence the work reported in the paper.

Data availability

The datasets generated and/or analysed during the study are available on reasonable request.
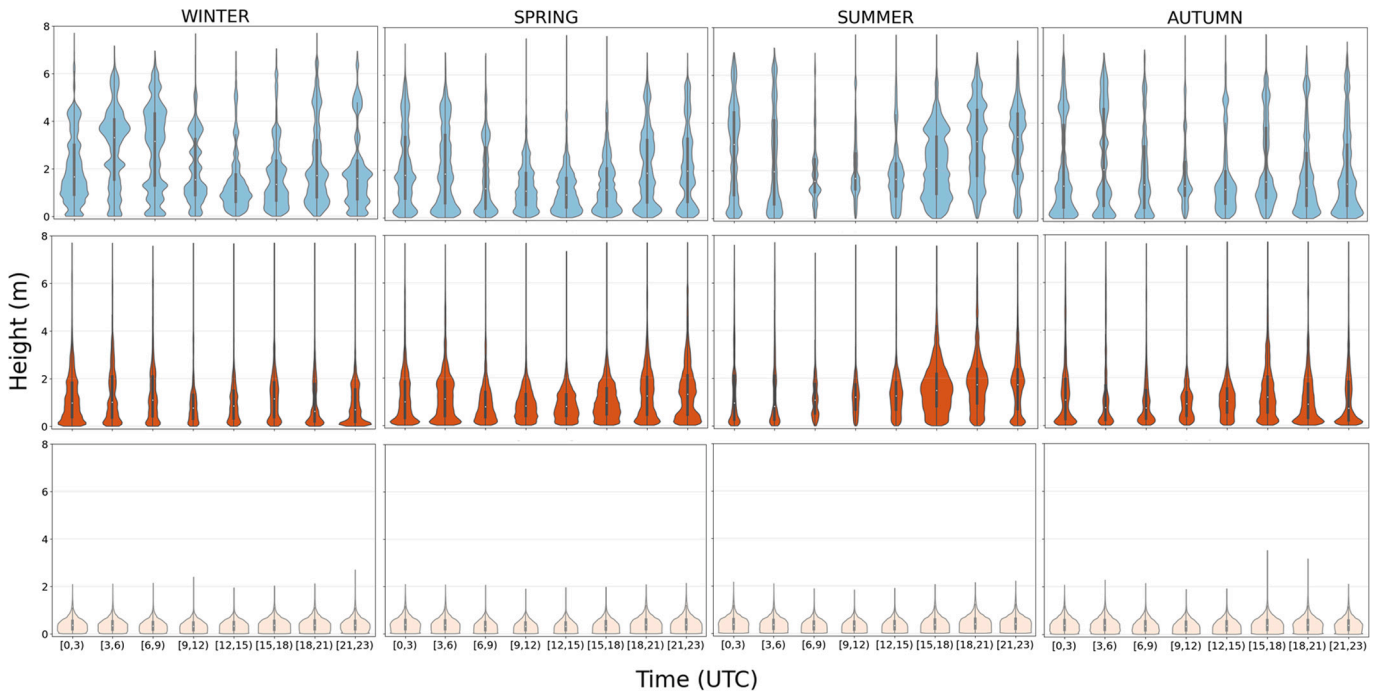
Acknowledgements

Appendix A. Annex

Fig. A1. Seasonal evolution of height-hour distribution for cloud, TZ and aerosol.
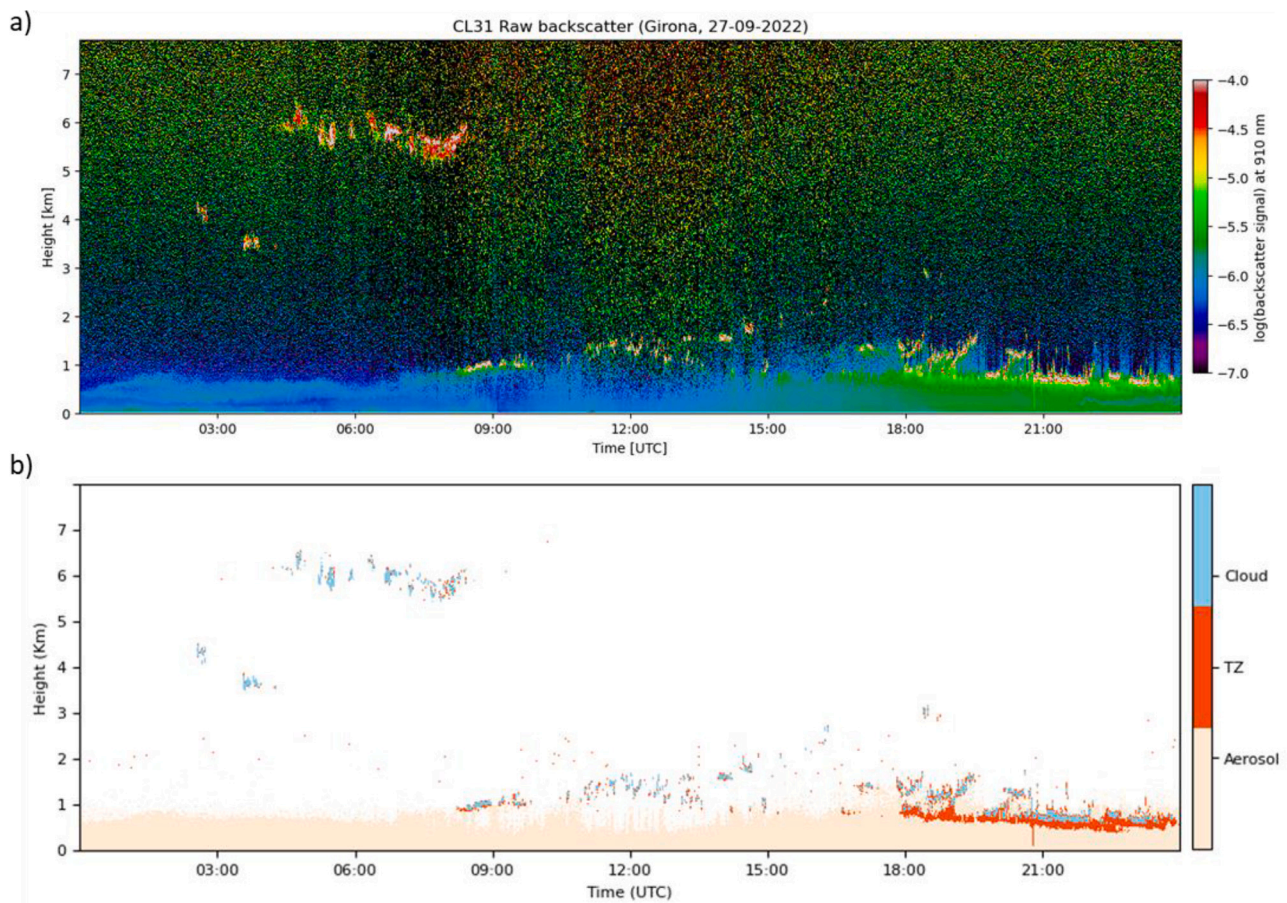
Appendix B. Annex

Fig. B1. Comparison between raw measurements and feature classification in the study case conducted in Girona on 27th September 2022. a) Raw backscatter profiles. Note that the signal is represented as the logarithm of the backscatter signal; b) Cloud, TZ and aerosol classification.

Appendix C. Glossary

ABL	atmospheric boundary layer
ACTRIS	aerosol clouds and trace gases research infrastructure
ALC	automatic low-power LiDAR and ceilometers
ALCF	automatic LiDAR and ceilometer framework
ALICENET	aerosol LiDAR ceilometer network
APD	avalanche photodiode
β	signal-to-noise ratio screened backscatter
β_{raw}	raw backscatter
β_{smooth}	signal-to-noise ratio screened backscatter with smoothed weak background
Bth	backscatter threshold
CBH	cloud base height
CC	cloud cover
CCN	cloud condensation nuclei
CLE	ceilometer engine board
CLR	ceilometer receiver board
CO	cloud occurrence
EUMETNET	European meteorological services network
InGaAs	indium gallium arsenide
IPCC	intergovernmental panel on climate change
LiDAR	light detection and ranging
PT	polar threshold
RCS	range corrected signal
SNR	signal-to-noise ratio
SNRth	signal-to-noise ratio threshold
SONA	Sistema de observación automático de nubes (automatic cloud observation system)
THT	temporal height tracking
TZ	transition zone

References

Ahrens, C.D., 2009. Meteorology Today: An Introduction to Weather, Climate, and the Environment, ninth ed.

Albrecht, B.A., 1989. Aerosols, cloud microphysics, and fractional cloudiness. Science 245 (4923), 1227–1230. https://doi.org/10.1126/SCIENCE.245.4923.1227.

Bedoya-Velásquez, A.E., Ceolato, R., Lefebvre, S., 2021. Optimal estimation method applied on ceilometer aerosol retrievals. Atmos. Environ. 249 https://doi.org/10.1016/J.ATMOSENV.2021.118243.

Bellini, A., Diémoz, H., Di Liberto, L., Gobbi, G.P., Bracci, A., Pasqualini, F., Barnaba, F., 2024. Alicenet – An Italian network of Automated Lidar-Ceilometers for 4D aerosol monitoring: infrastructure, data processing, and applications. EGUsphere [preprint]. https://doi.org/10.5194/egusphere-2024-730.

Calbó, J., Sanchez-Lorenzo, A., 2009. Cloudiness climatology in the Iberian Peninsula from three global gridded datasets (ISCCP, CRU TS 2.1, ERA-40). Theor. Appl. Climatol. 96 (1–2), 105–115. https://doi.org/10.1007/s00704-008-0039-z.

Calbó, J., Long, C.N., González, J.A., Augustine, J., McComiskey, A., 2017. The thin border between cloud and aerosol: Sensitivity of several ground-based observation techniques. Atmos. Res. 196 (May), 248–260. https://doi.org/10.1016/j.atmosres.2017.06.010.

Calbó, J., González, J.-A., Jahani, B., Sola, Y., Ruiz de Morales, J., 2024. How important is the transition zone between clouds and aerosol? AIP Conf. Proc. 2988, 070005 https://doi.org/10.1063/5.0182769.

Charlson, R.J., Ackerman, A.S., Bender, F.A.M., Anderson, T.L., Liu, Z., 2007. On the climate forcing consequences of the albedo continuum between cloudy and clear air. Tellus Ser. B Chem. Phys. Meteorol. 59 (4), 715–727. https://doi.org/10.1111/j.1600-0889.2007.00297.x.

Costa-Surós, M., Calbó, J., González, J.A., Martin-Vide, J., 2013. Behavior of cloud base height from ceilometer measurements. Atmos. Res. 127, 64–76. https://doi.org/10.1016/J.ATMOSRES.2013.02.005.

Diémoz, H., Bellini, A., Barnaba, F., di Liberto, L., Gobbi, G.P., 2022. The Italian Automated Lidar-Ceilometer Network (ALICEnet): infrastructure, algorithms and applications. EGUGA. https://doi.org/10.5194/EGUSPHERE-EGU22-6118. EGU22-6118.

Eytan, E., Koren, I., Altaratz, O., Kostinski, A.B., Ronen, A., 2020. Longwave radiative effect of the cloud twilight zone. Nat. Geosci. 13 (10), 669–673. https://doi.org/10.1038/s41561-020-0636-8.

Fuchs, J., Cermak, J., 2015. Where Aerosols become clouds-potential for global analysis based on CALIPSO data. Remote Sens. 7 (4), 4178–4190. https://doi.org/10.3390/RS70404178.

González, J.A., Calbó, J., 2020. Assessing rapid variability in atmospheric apparent optical depth with an array spectrometer system. Remote Sens. 12 (18), 2917. https://doi.org/10.3390/RS12182917.

González, J.A., Calbó, J., Sola, Y., 2023. Assessment of cloudless-to-cloud transition zone from downwelling longwave irradiance measurements. Atmos. Res. 285, 106657 https://doi.org/10.1016/J.ATMOSRES.2023.106657.

Haeffelin, M., Bergot, T., Elias, T., Tardif, R., Carrer, D., Chazette, P., Colomb, M., Drobinski, P., Dupont, E., Dupont, J.C., Gomes, L., Musson-Genon, L., Pietras, C., Plana-Fattori, A., Protat, A., Rangognio, J., Raut, J.C., Rémy, S., Richard, D., Sciare, J., Zhang, X., 2010. Parisfog: Shedding new Light on fog Physical Processes. Bull. Am. Meteorol. Soc. 91 (6), 767–783. https://doi.org/10.1175/2009BAMS2671.1.

Haeffelin, M., Laffineur, Q., Bravo-Aranda, J.-A., Drouin, M.-A., Casquero-Vera, J.-A., Dupont, J.-C., de Backer, H., 2016. Radiation fog formation alerts using attenuated backscatter power from automatic lidars and ceilometers. Atmos. Meas. Tech. 9, 5347–5365. https://doi.org/10.5194/amt-9-5347-2016.

Harrison, R.G., Nicoll, K.A., Marlton, G.J., Ryder, C.L., Bennett, A.J., 2018. Saharan dust plume charging observed over the UK. Environ. Res. Lett. 13 (5), 054018 https://doi.org/10.1088/1748-9326/AABCD9.

Illingworth, A.J., Hogan, R.J., O'Connor, E.J., Bouniol, D., Brooks, M.E., Delanoë, J., Donovan, D.P., Eastment, J.D., Gaussiat, N., Goddard, J.W.F., Haeffelin, M., Klein Baltink, H., Krasnov, O.A., Pelon, J., Piriou, J.M., Protat, A., Russchenberg, H.W.J., Seifert, A., Tompkins, A.M., Wrench, C.L., 2007. Cloudnet: continuous evaluation of cloud profiles in seven operational models using ground-based observations. Bull. Am. Meteorol. Soc. 88 (6), 883–898. https://doi.org/10.1175/BAMS-88-6-883.

Iqbal, M., 1983. An Introduction to Solar Radiation. Acad. Press. http://www.sciencedirect.com:5070/book/9780123737502/an-introduction-to-solar-radiation.

Jahani, B., Calbó, J., González, J.A., 2019. Transition zone radiative effects in shortwave radiation parameterizations: case of weather research and forecasting model. J. Geophys. Res. Atmos. 124 (23), 13091–13104. https://doi.org/10.1029/2019JD031064.

Jahani, B., Calbó, J., González, J.A., 2020. Quantifying transition zone radiative effects in longwave radiation parameterizations. Geophys. Res. Lett. 47 (22) https://doi.org/10.1029/2020GL090408.

Jahani, B., Andersen, H., Calbo, J., Gonzalez, J.A., Cermak, J., 2022. Longwave radiative effect of the cloud-aerosol transition zone based on CERES observations. Atmos. Chem. Phys. 22 (2), 1483–1494. https://doi.org/10.5194/ACP-22-1483-2022.

Khain, A., Pinsky, M., Eytan, E., Koren, I., Altaratz, O., Arieli, Y., Gavze, E., 2024. Dynamics and microphysics in small developing cumulus clouds. Atmos. Res. 307, 107454 https://doi.org/10.1016/j.atmosres.2024.107454.

Koren, I., Remer, L., Kaufman, Y.J., Rudich, Y., Martins, J.V., 2007. On the twilight zone between clouds and aerosols. Geophys. Res. Lett. 34 (8), 1–5. https://doi.org/10.1029/2007GL029253.

Koren, I., Oreopoulos, L., Feingold, G., Remer, L.A., Altaratz, O., 2008. How small is a small cloud? Atmos. Chem. Phys. Discuss. 8 (2), 6379–6407. https://doi.org/10.5194/acpd-8-6379-2008.

Kotthaus, S., Grimmond, C.S.B., 2018. Atmospheric boundary-layer characteristics from ceilometer measurements. Part 1: A new method to track mixed layer height and classify clouds. Quart. J. R. Meteorol. Soc. 144 (714), 1525–1538. https://doi.org/10.1002/QJ.3299.

Kotthaus, S., O'Connor, E., Münkel, C., Charlton-Perez, C., Haeffelin, M., Gabey, A.M., Grimmond, C.S.B., 2016. Recommendations for processing atmospheric attenuated backscatter profiles from Vaisala CL31 ceilometers. Atmos. Meas. Tech. 9 (8), 3769–3791. https://doi.org/10.5194/AMT-9-3769-2016.

Kotthaus, S., Haeffelin, M., Drouin, M.A., Dupont, J.C., Grimmond, S., Haefele, A., Hervo, M., Poltera, Y., Wiegner, M., 2020. Tailored algorithms for the detection of the atmospheric boundary layer height from common automatic lidars and ceilometers (ALC). Remote Sens. 12 (19), 3259. https://doi.org/10.3390/RS12193259.

Kuma, P., Mcdonald, A.J., Morgenstern, O., Querel, R., Silber, I., Flynn, C.J., 2021. Ground-based lidar processing and simulator framework for comparing models and observations (ALCF 1.0). Geosci. Model Dev. 14, 43–72. https://doi.org/10.5194/gmd-14-43-2021.

Lenoble, J., 1993. Atmospheric radiative transfer. A. Deepak Pub., Hampton, Va., USA.

Marcos, C., 2017. Determination of the Vertical Distribution of Aerosols in Valencia, Spain, by Means of Lidar Measurements. PhD thesis. Universitat de València. https://www.educacion.gob.es/teseo/imprimirFicheroTesis.do?idFichero=Rref6lHfmYY%3D.

Marcos, C.R., Gómez-Amo, J.L., Peris, C., Pedrós, R., Utrillas, M.P., Martínez-Lozano, J.A., 2018. Analysis of four years of ceilometer-derived aerosol backscatter profiles in a coastal site of the western Mediterranean. Atmos. Res. 213, 331–345. https://doi.org/10.1016/J.ATMOSRES.2018.06.016.

Martucci, G., Milroy, C., O'Dowd, C.D., 2010. Detection of cloud-base height using Jenoptik CHM15K and Vaisala CL31 ceilometers. J. Atmos. Ocean. Technol. 27 (2), 305–318. https://doi.org/10.1175/2009JTECHA1326.1.

Masson-Delmotte, V., Zhai, P., Pirani, A., Connors, S.L., Péan, C., Berger, S., Caud, N., Chen, Y., Goldfarb, L., Gomis, M.I., Huang, M., Leitzell, K., Lonnoy, E., Matthews, J.B.R., Maycock, T.K., Waterfield, T., Yelekçi, O., Yu, R., Zhou, B., IPCC, 2021. Climate Change 2021: The Physical Science Basis. Contribution of Working Group I to the Sixth Assessment Report of the Intergovernmental Panel on Climate Change. Camb. Univ. Press, Cambridge, United Kingdom and New York, NY, USA. https://doi.org/10.1017/9781009157896.

Mattis, I., Wagner, F., 2014. E-PROFILE: Glossary of lidar and ceilometer variables. Retrieved from: https://www.eumetnet.eu/wp-content/uploads/2016/10/ALC_glossary.pdf.

Münkel, C., Eresmaa, N., Räsänen, J., Karppinen, A., 2007. Retrieval of mixing height and dust concentration with lidar ceilometer. Bound.-Layer Meteorol. 124 (1), 117–128. https://doi.org/10.1007/S10546-006-9103-3.

Murray, B.J., Carslaw, K.S., Field, P.R., 2021. Opinion: Cloud-phase climate feedback and the importance of ice-nucleating particles. Atmos. Chem. Phys. 21, 665–679. https://doi.org/10.5194/acp-21-665-2021.

O'Connor, E., Illingworth, A., Hogan, R., 2004. A Technique for Autocalibration of Cloud Lidar. J. Atmos. Ocean. Technol. 21, 777–786. https://doi.org/10.1175/1520-0426(2004)021<0777:ATFAOC>2.0.CO;2.

O'Connor, E.J., Hogan, R.J., Illingworth, A.J., 2005. Retrieving stratocumulus drizzle parameters using doppler radar and lidar. J. Appl. Meteorol. Climatol. 44 (1), 14–27. https://doi.org/10.1175/JAM-2181.1.

Ramanathan, V., Cess, R.D., Harrison, E.F., Minnis, P., Barkstrom, B.R., Ahmad, E., Hartmann, D., 1989. Cloud-radiative forcing and climate: results from the earth radiation budget experiment. Science 243 (4887), 57–63. https://doi.org/10.1126/SCIENCE.243.4887.57.

Rieutord, T., Aubert, S., MacHado, T., 2021. Deriving boundary layer height from aerosol lidar using machine learning: KABL and ADABL algorithms. Atmos. Meas. Tech. 14 (6), 4335–4353. https://doi.org/10.5194/AMT-14-4335-2021.

Rogers, R.R., Lamoureux, M.-F., Bissonnette, L.R., Peters, R.M., 1997. Quantitative interpretation of laser ceilometer intensity profiles. J. Atmos. Ocean. Technol. 14, 396–411. https://doi.org/10.1175/1520-0426(1997)014<0396:QIOLCI>2.0.CO;2.

Román, R., Cazorla, A., Toledano, C., Olmo, F.J., Cachorro, V.E., de Frutos, A., Alados-Arboledas, L., 2017. Cloud cover detection combining high dynamic range sky images and ceilometer measurements. Atmos. Res. 196, 224–236. https://doi.org/10.1016/J.ATMOSRES.2017.06.006.

Rosenfeld, D., Sherwood, S., Wood, R., Donner, L., 2014. Climate effects of aerosol-cloud interactions. Science 343 (6169), 379–380. https://www.science.org/doi/10.1126/science.1247490.

Sanchez-Romero, A., González, J.A., Calbó, J., Sanchez-Lorenzo, A., Michalsky, J., 2016. Aerosol optical depth in a western Mediterranean site: an assessment of different methods. Atmos. Res. 174–175, 70–84. https://doi.org/10.1016/J.ATMOSRES.2016.02.002.

Schwarz, K., Cermak, J., Fuchs, J., Andersen, H., 2017. Mapping the twilight zone-what we are missing between clouds and aerosols. Remote Sens. 9 (6) https://doi.org/10.3390/RS9060577.

Simpkins, G., 2018. Aerosol–cloud interactions. Nat. Clim. Ch. 8 (6), 457. https://doi.org/10.1038/s41558-018-0195-9.

Sola, Y., González, J.A., Calbó, J., 2024. Radiative effects of aerosol-cloud transition zone in radiative transfer models: a sensitivity analysis. J. Geophys. Res. Atmos. (submitted).

Toledo, F., Haeffelin, M., Waersted, E., Dupont, J.-C., 2021. A new conceptual model for adiabatic fog. Atmos. Chem. Phys. 21, 13099–13117. https://doi.org/10.5194/acp-21-13099-2021.

Tukiainen, S., O'Connor, E., Korpinen, A., 2020. CloudnetPy: A Python package for processing cloud remote sensing data. J. Open Source Softw. 5 (53), 2123. https://doi.org/10.21105/JOSS.02123.

Tuononen, M., O'Connor, E.J., Sinclair, V.A., 2019. Evaluating solar radiation forecast uncertainty. Atmos. Chem. Phys. 19 (3), 1985–2000. https://doi.org/10.5194/ACP-19-1985-2019.

Twohy, C.H., Coakley, J.A., Tahnk, W.R., 2009. Effect of changes in relative humidity on aerosol scattering near clouds. J. Geophys. Res. Atmos. 114 (5) https://doi.org/10.1029/2008JD010991.

Twomey, S., 1974. Pollution and the planetary albedo. Atmos. Environ. 8 (12), 1251–1256. https://doi.org/10.1016/0004-6981(74)90004-3.

Van Tricht, K., Gorodetskaya, I., Lhermitte, S., Turner, D.D., Schween, J.H., van Lipzig, N.P.M., 2014. An improved algorithm for polar cloud-base detection by ceilometer over the ice sheets. Atmos. Meas. Tech. 7 (5), 1153–1167. https://doi.org/10.5194/AMT-7-1153-2014.

Várnai, T., Marshak, A., 2009. MODIS observations of enhanced clear sky reflectance near clouds. Geophys. Res. Lett. 36 (6), L06807. https://doi.org/10.1029/2008GL037089.

Várnai, T., Marshak, A., 2011. Global CALIPSO observations of aerosol changes near clouds. IEEE Geosci. Remote Sens. Lett. 8 (1) https://doi.org/10.1109/LGRS.2010.2049982.

Wallace, J.M., Hobbs, P., v., 2006. Atmospheric Science: An Introductory Survey, Second edition. Elsevier Inc., pp. 1–488. https://doi.org/10.1016/C2009-0-00034-8

Wang, R., Balkanski, Y., Boucher, O., Ciais, P., Schuster, G.L., Chevallier, F., Samset, B. H., Liu, J., Piao, S., Valari, M., Tao, S., 2016. Estimation of global black carbon direct radiative forcing and its uncertainty constrained by observations. J. Geophys. Res. Atmos. 121 (10), 5948–5971. https://doi.org/10.1002/2015JD024326.

Wen, G., Marshak, A., 2022. Precipitable water vapor variation in the clear-cloud transition zone from the ARM shortwave spectrometer. IEEE Geosci. Remote Sens. Lett. 19 https://doi.org/10.1109/LGRS.2021.3064334.

Wiegner, M., Madonna, F., Binietoglou, I., Forkel, R., Gasteiger, J., Geiß, A., Pappalardo, G., Schäfer, K., Thomas, W., 2014. What is the benefit of ceilometers for aerosol remote sensing? An answer from EARLINET. Atmos. Meas. Tech. 7 (7), 1979–1997. https://doi.org/10.5194/AMT-7-1979-2014.

Yang, F., Kostinski, A.B., Zhu, Z., Lamer, K., Luke, E., Kollias, P., Sua, Y.M., Hou, P., Shaw, R.A., Vogelmann, A.M., 2024. A single-photon lidar observes atmospheric clouds at decimeter scales: resolving droplet activation within cloud base. Npj Clim. Atmos. Sci. 7 (1), 92. https://doi.org/10.1038/s41612-024-00644-y.

Yano, J.I.I., Ziemian'ski, M.Z., Cullen, M., Termonia, P., Onvlee, J., Bengtsson, L., Carrassi, A., Davy, R., Deluca, A., Gray, S.L., Homar, V., Köhler, M.I., Krichak, S., Michaelides, S., Phillips, V.T.J., Soares, P.M.M., Wyszogrodzki, A.A., 2018. Scientific challenges of convective-scale numerical weather prediction. Bull. Am. Meteorol. Soc. 99 (4), 699–710. https://doi.org/10.1175/BAMS-D-17-0125.1.